Photovoltaic Performance of Phase-Pure Orthorhombic BiSI Thin-Films

Devendra Tiwari,[1] Fabiola Cardoso-Delgado,[1,2] Dominic Alibhai,[3] Maia Mombrú,[2,4] and David J. Fermín[1,2]*

[1]School of Chemistry, Cantocks close, University of Bristol, Bristol BS8 1TS, UK

[2]Bristol Centre for Functional Nanomaterials, HH Wills Physics Laboratory, University of Bristol, Tyndall Avenue, Bristol, BS8 1TL, UK

[3]Wolfson Bioimaging Facility, Faculty of Biomedical Sciences, University of Bristol, University Walk, Bristol BS8 1TD, UK

[4]Current address: Grupo de Desarrollo de Materiales y Estudios Ambientales, Área Radioquímica, Departamento Estrella Campos, Facultad de Química, Universidad de la República, Montevideo 11800, Uruguay

*Corresponding author: David.Fermin@bristol.ac.uk

ABSTRACT

A single-precursor solution approach is developed for depositing stoichiometric BiSI thin films featuring pure paraelectric orthorhombic (Pnam) phase. The compact and homogenous films are composed of flake-shaped grains oriented anti-planar to the substrate and display a sharp optical transition corresponding to a bandgap of 1.57 eV. Optical and Raman signatures of the thin films are rationalized using the quasiparticle G_0W_0@PBE0 and Density Functional Perturbation Theory calculations. Electrochemical impedance spectroscopy revealed n-type doping with valence and conduction band edges located at 4.6 and 6.2 eV below vacuum level, respectively. Planar BiSI solar cells are fabricated with the architecture: glass/FTO/SnO2/BiSI/F8/Au, where F8 is poly(9,9-di-n-octylfluorenyl-2,7-diyl), showing record conversion efficiency of 1.32% under AM 1.5 illumination.

Keywords: BiSI, Thin-Film, Photovoltaic, Power Conversion Losses, Band Structure, G_0W_0@PBE0

INTRODUCTION

One of the grand challenges in the field of photovoltaic materials is to design stable materials which reproduce the outstanding optoelectronic properties of lead organo-halide perovskites (LOHPs), such as: (i) > 1 μm diffusion lengths, (ii) ~1 μs carrier lifetimes, (iii) carrier mobility > 10 $cm^2V^{-1}s^{-1}$.[1,2] These remarkable properties, observed regardless of the preparation method, emerge from the inherent defect-tolerant electronic structure featuring no intrinsic deep trap states, large band dispersion, and enhanced spin-orbit coupling.[3,4] Defect tolerance in LOHPs is associated with the partially oxidized Pb^{2+} cation. Interestingly, similar arguments can be made about other polarizable cations with the ns^2 lone pair such as In^+, Sn^{2+}, Sb^{3+}, Tl^+, Bi^{3+}.[5,6]

Based on this concept, Bi-based compounds such as $AgBiS_2$, $BiFeO_3$, and Bi_2S_3 have been considered as solar absorbers, delivering power conversion efficiencies between 3.3 and 6.3 %.[7–11] Bi halides have also been investigated including BiI_3 (1.2%),[12] $Cs_2AgBiBr_6$ (2.43%),[13] and $AgBi_2I_7$ (1.2%).[6,10,11,14] In addition to defect tolerance, materials such as BiOI and BiSI are also characterized by polar crystal structures featuring photoferroic properties and paraelectric phases with large dielectric constants.[15–19] The performance of BiOI solar cells have progressed from ~ 0.1% to 1.8 % within last 8 years.[20–23] Mullins and co-workers have reported photoelectrochemical and solid-state BiSI cells displaying efficiencies of 0.012% and 0.25%, respectively.[24,25] Considering the lower band gap (1.57 eV) and large absorption cross-section of BiSI,[26] in comparison to BiOI (1.9-2.0 eV),[23] one might expect the former to exhibit better PV performance.

One of the key challenges in fabricating high-performance BiSI solar cells is the presence of secondary phases. The ternary phase diagram of Bi-S-I features 4 ternary and over 15 binary

stable compositions, thus obtaining pure BiSI film in the required 1:1:1 elemental atomic ratio is non-trivial.[24,27,28] Designing an optimal cell architecture with a well-aligned electron (ETL) and hole-transporting layers (HTL) is another important challenge. In this report, we describe a new solution-based approach, leading to paraelectric BiSI films with a very high degree of phase purity as confirmed by quantitative XRD and Raman analysis. Optical and electrochemical measurements, complemented by electronic structure calculations, provided information on band gap and the band edge energy positions. These measurements guided the design of a solid-state cell featuring SnO_2 as ETL and poly(9,9-di-n-octylfluorenyl-2,7-diyl) (F8) as HTL, showing record conversion efficiency of 1.3% under AM 1.5 illumination. We discuss potential power conversion losses associated with deep trap states linked to charged sulfur vacancies.

RESULTS AND DISCUSSION

The synthesis of phase-pure BiSI thin films was achieved by thermolysis of a single molecular precursor consisting of $Bi(NO_3)_3.5H_2O$, thiourea and NH_4I in 2-methoxyethanol and acetylacetone (4:1) (exact compositions are given in the Experimental Section). As we have demonstrated in previous studies on kesterite and chalcopyrite absorbers, tuning solvent mixtures provide better wettability and much higher solubility which is crucial to ensure homogeneous film composition.[29–32] Indeed, we were not able to generate phase-pure material employing a glycol-based precursor used in previous works.[24] The highly concentrated molecular precursor solution is spin-coated onto the substrate and heated at 200 ^oC in the air, yielding a homogenous and adherent film. The thermolysis temperature is another key factor, with the possibility of partial oxidation above 250 ^oC.

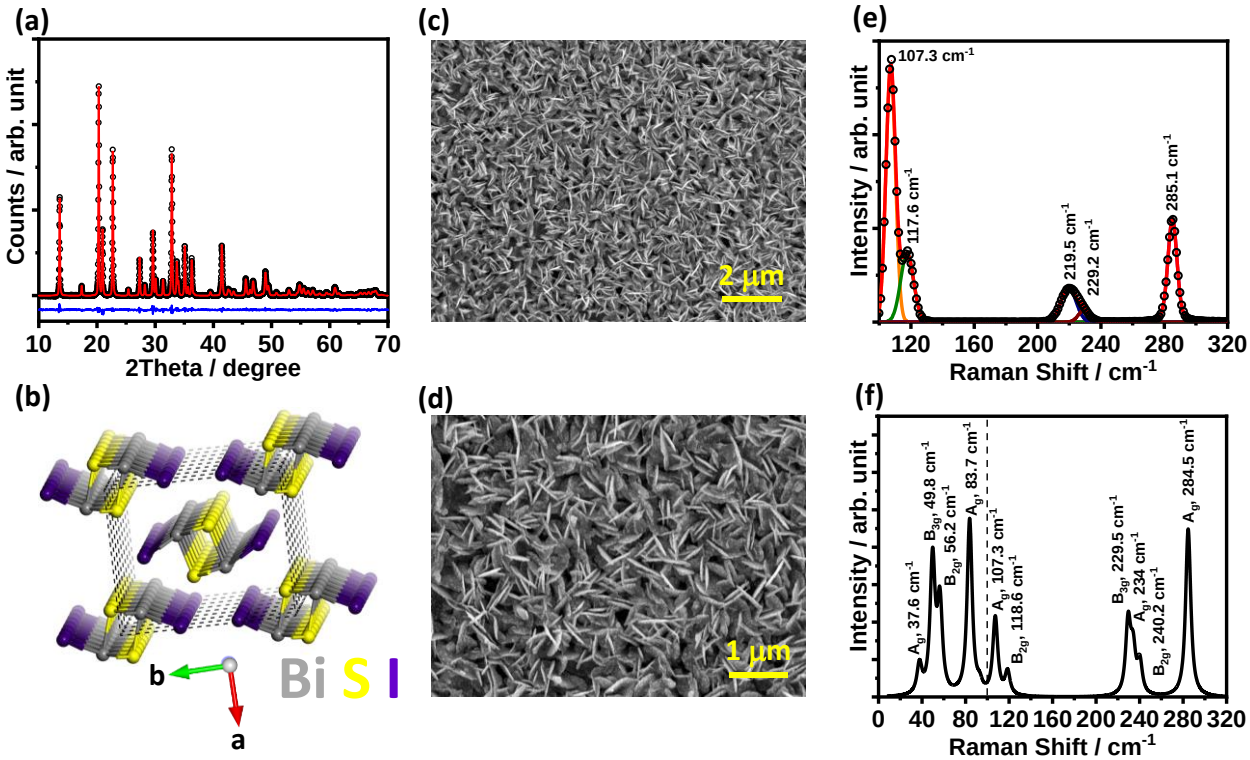

Figure 1: Structure and morphology of as-grown BiSI films: (a) X-ray diffraction and unit cell structure refined using the Rietveld approach; (b) BiSI structure obtained from refinement as seen along the c-axis; (c - d) top-view scanning electron micrograph displaying flake-shaped grains at two different magnifications; (e) Raman spectrum measured under 785 nm excitation and deconvoluted using five modes at 107, 118, 220, 229 and 285 cm^{-1}; (f) theoretical Raman spectrum of the BiSI phase featuring a D_{2h} point group symmetry, calculated by density functional perturbation theory. The dashed line delimits the experimentally accessible range.

The characteristic X-ray Diffraction (XRD) pattern, film morphology and Raman spectrum of the BiSI films are illustrated in **Figure 1**. As shown in **Figure 1a**, quantitative structure

refinement using Rietveld method shows an excellent fit to the orthorhombic BiSI (space group: Pnam), with correlation indices R_p and R_{wp} of 3.64 % and 6.35 %, respectively. No other peaks associated with secondary phases such as Bi_2S_3, BiI_3 or BiOI are identified in the diffractogram. The refined structural parameters including the atomic positions are provided in the supplementary information **Table S1**, while the crystallographic information file (CIF) can be accessed through the Cambridge Structural Database (CCDC 1898290). The lattice parameters of the final structure are a = 8.3881(14) Å, b = 10.1099(16) Å and c = 4.1156(7) Å, which are in very good agreement with previously reported data on single BiSI crystals.[33–35] The relative elemental composition of Bi:S:I as estimated from the atomic occupancies 1:0.95:0.97, respectively. This stoichiometry is consistent with Energy Dispersive Analysis of X-rays (EDX, data not shown), yielding an elemental ratio of 1.04:0.94:0.98, respectively. **Figure 1b** shows the stacks of unit cells of the refined structure along the c-axis. The BiSI structure consists of c-axis aligned $(Bi_2S_2I_2)_n$ chains with Bi-S distances of 2.539(5) Å and 2.726(3) Å; and Bi-I distances of 3.6893(12) Å and 3.1586(12) Å. These chains are held together by weak van der Waals interactions. The SEM micrograph in **Figure 1c and d** show uniformly distributed flake-shaped grains with sharp edges and sizes between 600 and 700 nm, oriented antiparallel to the substrate. The flake-like nature of the grain can be rationalized in terms of the bunching of the $(Bi_2S_2I_2)_n$ chains in the yz-plane.

As-grown BiSI films exhibit well-defined Raman bands as shown in **Figure 1e**, which can be deconvoluted into five modes at 107, 118, 220, 229 and 285 cm^{-1}. In order to rationalize these Raman modes, we carried out density functional perturbation theory (DFPT) calculations leading to the spectrum shown in **Figure 1f**. The dashed line in **Figure 1f** represents the lower wavenumber limit available experimentally. To the best of our knowledge, first-principles

calculations of vibrational properties of BiSI have not been reported yet, with previous studies relying on qualitative group theoretic normal mode analysis.[36] The measured bands found to have a one-to-one correspondence with the calculated Raman spectrum, which further confirms the paraelectric BiSI phase (D_{2h} point group symmetry). The calculated spectrum also coincides well with previous measurements on BiSI single crystals in the range of 10 cm^{-1} to 300 cm^{-1}.[17] As mentioned above, the ternary phase diagram of Bi-S-I is composed of 4 ternary and over 15 binary thermodynamically stable compositions simultaneously competing during the synthesis. The ensemble of data shown in **Figure 1** clearly demonstrates the formation of pure BiSI in paraelectric orthorhombic structure, devoid of secondary composition and structural phases.

Figure 2a shows the transmittance and reflectance spectra of a 150 nm thick BiSI films, showing a sharp absorption edge close to 800 nm. The highly textured morphology generates diffuse scattering of photons below 1.5 eV. As the indirect and direct band gaps in BiSI are very close (see discussion below),[16,37] absorption at 1.57 eV is expected to be dominated by direct optical transitions, leading to an absorption coefficient in the range of 5 $x10^4$ cm^{-1}. The calculated absorption coefficient is plotted as a function of incident photon energy in **Figure 2b**. A band gap of 1.57 eV is determined from extrapolating the sharp absorption edge, which is in good agreement with optical measurements performed on single crystals.[19,37] The complex nature of the band edges in this material, which is discussed further below, prevents the use of conventional approaches such as Tauc's plot for band gap estimations. Indeed, Tauc's plot can be justified *if* average momentum matrix element square remains independent of photon energy *and only if* density of states at band edge vary as either square (direct transition) or square-root function of energy (indirect transition).[38] **Figure S1** shows that depending on the function used, band gap values of 1.62 and 1.50 eV can be obtained assuming either direct or indirect

transitions. **Figure 2b** also displays the room temperature photoluminescence (PL) spectrum, measured with a 2.41 eV excitation source, featuring a peak centered at 1.56 eV. This observation further supports our direct analysis of the absorption edge transition from the absorption spectrum.

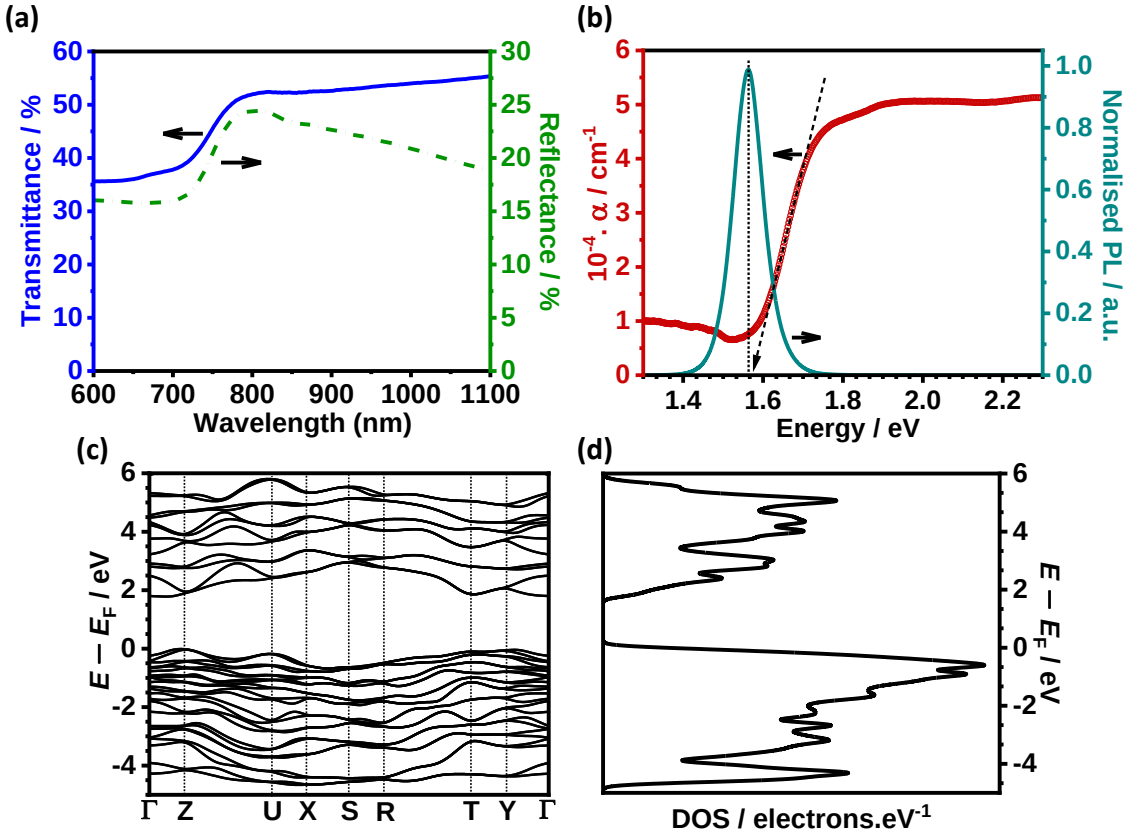

Figure 2: Optical properties and electronic structure of BiSI: (a) Transmittance and reflectance spectra of 150 nm BiSI films as grown onto 2.5 × 2.5 cm^2 glass substrate; (b) calculated absorption coefficient (α) as a function of photon energy and room temperature photoluminescence spectrum of BiSI films upon 2.41 eV (514 nm) excitation source, establishing a direct absorption edge at 1.57 eV; (c) Band structure and (d) and density of states of paraelectric BiSI calculated employing GW@PBE0 formalism. The valence band minimum (VBM) and conduction band maximum (CBM) are situated at points between Γ–Y and Γ–Z paths, respectively.

The band structure and density of states (DOS) of BiSI, as calculated by GW@PBE0 are displayed in **Figure 2 c** and **d**, respectively. The many-body perturbation theory as formulated in quasiparticle GW approximation is the most rigorous method for the calculations of electronic structure, with non-selfconsistent single-shot G_0W_0 approximation being the simplest and least expensive to implement.[39] Results from G_0W_0 are rather sensitive to the starting point, with the hybrid functional PBE0 considered the most accurate.[40] Computational methods are described in the Computational Details section. **Figure 2c** shows that fundamental band gap transition at 1.77 eV (at 0K) is indirect, while a direct band gap transition is observed at 20 meV higher energy. Our calculations closely agree with those reported by Ganose et al. based on hybrid functional DFT (HSE06) as well as the empirical quasiparticle self-consistent GW formalisms.[16,41] The difference between calculated and experimental band gap can be largely rationalised in term of electron-phonon coupling effects at room temperature. The temperature coefficient of the bandgap of single crystal BiSI has been reported to be -7×10^{-4} eV/K.[26] Thus, the band gap is expected to decrease from 1.77 eV calculated at 0K to 1.56 eV at 300K, in excellent agreement with the measured value in as-deposited films. The spectral overlap of indirect and direct optical transitions is also observed in high performing absorbers such as methylammonium lead perovskite, which has been used to rationalize long carrier lifetimes.[42] The conduction band is significantly more disperse than the valence balance due to spin-orbit coupling effects induced by Bi^{3+}, resulting in a smaller effective mass of electrons ($m_e^* = 0.53\ m_0$) in comparison to holes ($m_h^* = 0.95\ m_0$). The variation of effective masses along the crystal directions are tabulated in **Table S2**, reflecting the anisotropic electronic structure of BiSI. We have also calculated the ionization potential (IP) of the films as 6.33 eV following the approached described by Carter

and co-workers.[43] As discussed below, we shall use this information to identify ETL and HTL with appropriate band alignment.

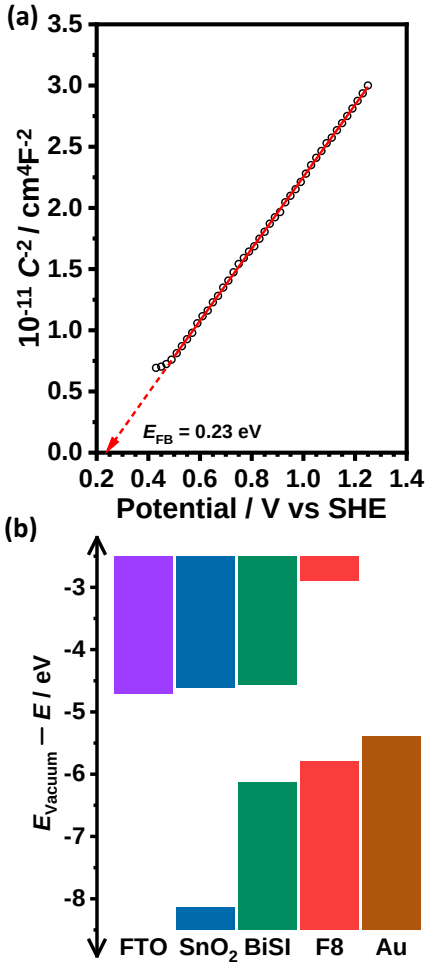

Figure 3: Band edges of BiSI and device band alignment: (a) Mott-Schottky plot of a BiSI film grown on FTO coated glass substrates in contact with a dichloromethane-based electrolyte solution. Details of the experimental conditions, including the reference potential scale can be found in the Experimental Details section. The interfacial capacitance is extracted from fitting electrochemical impedance spectra recorded between 7 and 4700 Hz. The flat band potential E_{FB} = 0.23 vs SHE corresponds to a CBM energy value of 4.67 eV vs vacuum. (b) Suggested band alignment of the F:SnO_2/SnO_2/BiSI/F8/Au solar cell based on measured EIS data for BiSI and SnO_2.

Figure 3a shows the potential dependence of the interfacial capacitance normalized by the geometric area of the BiSI film, employing the Mott-Schottky representation, as obtained from electrochemical impedance spectroscopy. Due to the poor stability of BiSI in aqueous electrolytes, a dichloromethane-based electrolyte is used as described in Experimental Details. The plot exhibits a highly linear trend over a potential range of more than 0.8 V, with a positive slope consistent with n-type conductivity. Employing a thermodynamic analysis for this electrolyte reported elsewhere,[44] the flat band potential of BiSI is estimated at 0.23 V vs SHE, which corresponds to CBM located at 4.67 eV vs vacuum. From the estimated optical band gap of 1.57 eV and the calculated IP, the VBM position is estimated to be located at 6.24 eV, which is close to the value extracted from the GW@PBE0 calculations mentioned above. Based on these values, which are also consistent with UPS analysis reported by Hahn et al.,[25] a device structure of glass/F:SnO_2/SnO_2/BiSI/F8/Au can be envisaged with the band alignment displayed in **Figure 3b**.[45–47] Capacitance measurements of the SnO_2 layer (see Experimental details and **Figure S2**) suggest an excellent conduction band alignment with BiSI, while a VBM offset of approximately 0.3 eV is predicted with respect to F8. According to this analysis, these devices feature a maximum built-in voltage larger than 1 V.

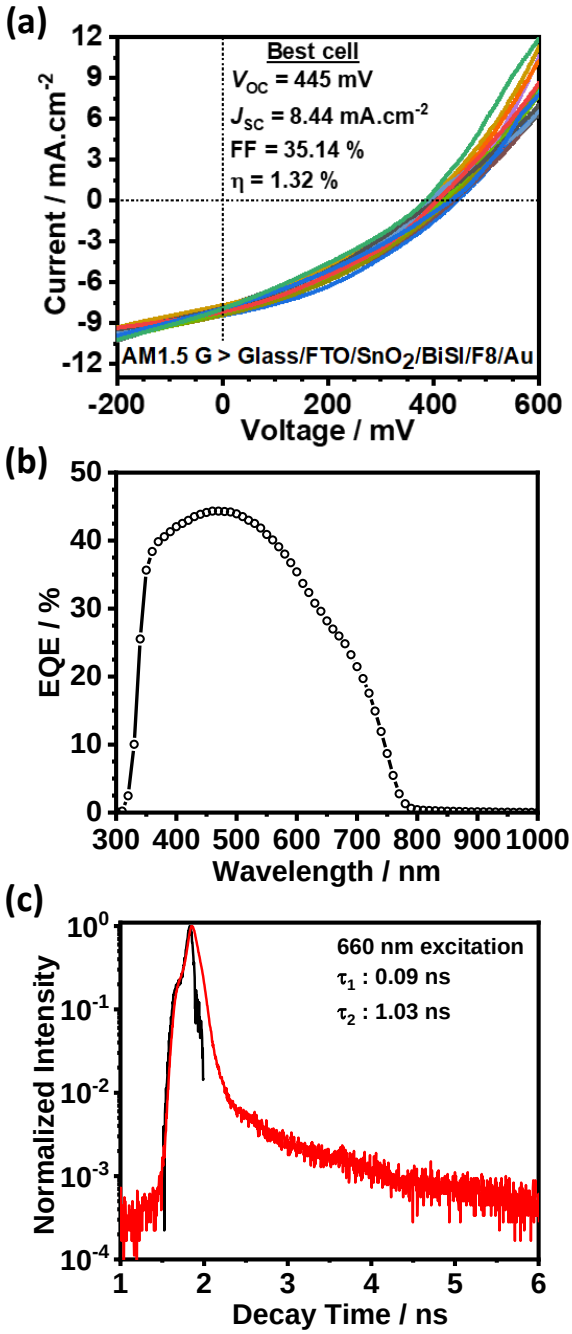

Figure 4: **PV performance of devices with the architecture glass/F:SnO2/SnO2/BiSI(150nm)/F8/Au**: (a) J-V characteristics of 16 devices under AM 1.5G simulated illumination and key performance metrics of the best device; (b) External quantum efficiency (EQE) spectrum of the champion device; (c) Time-resolved photoluminescence of BiSI films employing 660 nm excitation, revealing two time-constants of 0.09 and 1.03 ns.

J-V characteristics of 16 devices, with a BiSI film thickness of 150 nm, under simulated AM 1.5G spectrum (100mW/cm^2), are shown in **Figure 4a**. The best-performing device features a short-circuit current density (J_{SC}) of 8.44 mA/cm^2, open-circuit voltage (V_{OC}) of 445 mV, fill factor (FF) of 35.14 % and overall power conversion efficiency of 1.32 %. The latter value is more than 5 times larger than the best cell recorded for BiSI.[24] The dispersion of device parameters is tabulated in **Table S3**, which display a narrow distribution of 10 % in the performance. The spectral response of the best solar cell is presented in **Figure 4b**. The external quantum efficiency (EQE) spectrum is damped by the absorption of SnO_2 at wavelengths shorter than 340 nm. A band gap of 1.57 eV can be extracted from the absorption edge of BiSI (**Figure S3**), in agreement with the optical measurements (**Figure 2b**). The drop in EQE values at a wavelength longer than 580nm could be an indication of short minority-carrier lifetimes.

Figure 4c shows time-resolved photoluminescence decay of BiSI films, featuring a bi-exponential decay with lifetimes of τ_1 = 0.09 and τ_2 = 1.03 ns. As reported by Repins et al., device efficiencies exhibit a sharp dependence on carrier lifetimes below 10 ns,[48] which is also responsible for the decay in EQE towards the absorption onset (**Figure 4b**). These short carrier lifetimes along with the high series resistance and low shunt resistances could not only lead to ineffective charge *collection* but also charge *separation*, limiting both J_{SC} and V_{OC}. The high series resistance and low shunt resistances in the devices could be arising from the complex transport properties of BiSI, porous morphology and inhomogeneous F8 coverage. As discussed earlier, the preferential packing of the BiSI flakes in the film orients the crystal axis with higher carrier mobility (low carrier effective mass: m_{zz}) normal to the surface. However, the porous nature of the film suggests that BiSI/F8 boundary primarily forms along the direction of low carrier mobility (high carrier effective mass: m_{xx}). Indeed, similar effects have been seen in the

device based on Sb_2Se_3 grown as 1-dimensional nanoribbons.[49] Consequently, we predict that careful optimization of the BiSI film morphology will result in a significant improvement in device performance.

Finally, despite fulfilling several descriptors associated with defect-tolerance, the PL and PV performances of our material suggest the presence of bulk recombination centers. In a recent report, Bi_S and V_S (i.e. sulfur vacancy) point defects have been calculated as the most probable in Bi-rich and S-poor conditions films, creating mid-gap states that could act as recombination centres.[41] This point is also consistent with the extended criteria of defect tolerance based on crystal site symmetry and anion coordination argument recently exposed by Kurchin et al.[50] Both S and I are in low coordination state and cannot be ascribed to separate sub-structures. As illustrated in **Figure 1b**, BiSI is composed of 1-dimensional $(Bi_2S_2I_2)_n$ chains with two smaller sulfur atoms forming a bridge separating the two Bi^{+3} ions. This leads to large relaxations of adjacent atoms in the presence of charged sulfur vacancies, leading to deep traps.[41]

CONCLUSIONS

In conclusion, pure polycrystalline orthorhombic BiSI films with a high degree of phase purity have been prepared by thermolysis of a single molecular precursor. The films are composed of flake-shaped grains stacked in highly compact films over lengths of several micrometers. The phase purity was confirmed by quantitative structural refinement of XRD data and modelling Raman spectra using DFPT. A band gap of 1.57 eV was estimated by diffuse reflectance spectra, which bodes well with GW@PBE0 calculations. Guided by first principle calculation and electrochemical experiments, we designed PV devices with the architecture glass/F:SnO_2/SnO_2/BiSI/F8/Au, yielding a record power conversion of 1.32% under AM 1.5G

illumination. The power conversion losses were linked to carrier lifetimes of the order of 1 ns as probed by time-resolved photoluminescence at room temperature. We consider bulk point defects such as Bi_S and sulfur vacancies as potential bulk recombination sites. Consequently, in order to fully exploit the potential of this promising Earth-abundant solar absorber, further studies probing the nature of bulk defects are required as well as improving carrier extraction rates from ETL and HTL layers.

EXPERIMENTAL DETAILS

BiSI films are deposited on 2.5 × 2.5 cm^2 sized glass and fluorine doped tin oxide (FTO) coated glass substrates using molecular precursor approach. The precursor solution is prepared by dissolving $Bi(NO_3)_3.5H_2O$ (0.5 M), thiourea (1 M) and ammonium iodide (1 M), in a 2-methoxyethanol (4 parts) and acetylacetone (1 part) solvent mixture. Clean substrates are spin-coated with single precursor solution at 2000 rpm for 60 s, followed by heating at 200 ºC in the air for 5 minutes to promote the formation of BiSI. Previously reported glycol-based precursor solutions were investigated,[24] resulting in significantly less phase-pure films. The solvent mixture described here was carefully adjusted for not only achieving stable and concentrated solutions, but also appropriate wetting of the FTO coated glass. This is a key aspect in the preparation of homogenous and adherent pure phase films, with the desired thickness only after a single spin-coat. Thermolysis of the molecular precursor was promoted at 200 ºC, which is lower than in previous approaches based on spray pyrolysis.[24] Keeping the conversion temperature as low as possible minimize the formation of oxide phases.

Solar cells are fabricated with the architecture glass/F:SnO_2/SnO_2/BiSI/F8/Au, where F8 is Poly(9,9-di-n-octylfluorenyl-2,7-diyl. Cleaned FTO glass substrate (2.0 × 1.0 cm^2) is first spin-

coated with an ethanolic solution of tin (II) chloride dihydrate at 2000 rpm for 30 s and heated at 250 ^{o}C for 1 hour to form a SnO_2 layer acting as ETL. Following the thermolysis of BiSI, F8 is deposited by spin-coating 10 mg/mL solution in chlorobenzene at 2000 rpm for 30 s. The top contacts are laid by evaporating Au through shadow masks. All the chemicals used are of analytical reagent grade.

X-ray diffraction of BiSI films is measured in a powder diffractometer (Bruker D8 advance) fitted with Cu Kα source and a position sensitive Lynxeye detector. The scanning electron micrographs of films are acquired using a Jeol iT-300 microscope at 20 kV accelerating potential. The elemental analysis is performed through energy dispersive analysis of X-rays (EDAX) enabled by Oxford X-max 80 mm^2 silicon drift detector fitted in the SEM system. Raman and photoluminescence spectroscopies are performed in a Renishaw inVia spectrometer employing a 785 nm and 514 nm diode laser excitation sources, respectively. Diffuse reflectance spectrum is measured with a Shimadzu UV-2600 spectrophotometer in 600-1100 nm wavelength range at 1 nm steps.

Electrochemical impedance spectroscopy for BiSI films grown on FTO electrodes was recorded in the range of 7 to 4700 Hz with a potential modulation of 11 mV rms, using a Solatron Modulab system. The electrolyte used in these experiments is tetra-butylammonium hexafluorophosphate (NBu_4PF_6) in dichloromethane, with Pt and Ag wires used as counter and pseudo-reference electrodes. The potential scale is corrected against the standard hydrogen electrode (SHE) using the formal potential of ferrocene introduced as internal reference.[44] The films display a purely capacitive response under these conditions.

The Mott-Schottky plot of BiSI film in dichloromethane electrolyte containing NBu_4PF_6 is shown in **Figure 3a** of the paper. The flat band potential (E_{FB}) is estimated from the intercept of the linear portion according to the expression:

$$\frac{1}{C^2} = \frac{2}{A^2 q \varepsilon \varepsilon_o N_D}\left[(E - E_{FB}) - \frac{kT}{q}\right]$$

where A is the geometric surface area (1 cm^2), ε and ε_0 are the relative permittivities of BiSI (38 as estimated from DFT) and of free space, respectively. The positive slope of the plot confirms n-type conduction and a flat band potential (E_{FB}) of 0.23 V vs SHE is obtained from the x-intercept. The location of flat-band in reference to Vacuum is calculated considering SHE as 4.44 eV with respect to Vacuum. Donor density (N_D) is estimated to be 1.2 $x10^{19}$ cm^{-3}. However, N_D is expected to be significantly overestimated considering the highly textured topography of the films, increasing the effective surface area.

J-V characteristics of the solar cells are measured under a simulated AM1.5G (100 mW/cm^2) illumination employing an ABET technologies class ABA solar simulator. The active area of the devices is defined by a 4 mm^2 square aperture. The external quantum efficiency (EQE) spectrum of the best device is collected with a custom-built setup equipped with a Bentham TM 300 monochromator; and quartz halogen and Xenon lamps. The light sources are calibrated using an NREL certified Si photodiode from Newport Corporation. Time-resolved photoluminescence of BiSI films is acquired from a 10 μm^2 area at 25 ^oC upon 633 nm excitation. Using a time-correlated single photon counting system incorporated in a TCS SP8 system coupled to Leica DMi8 inverted microscope, the lifetime decays are collected in 4 ps bins.

COMPUTATIONAL DETAILS

Geometry optimization of BiSI unit cell is performed using CASTEP code, with energy and force convergences down to 1 x 10^{-9} eV/atom and 0.001 eV/Å, respectively.[51,52] PBE functional including Grimme dispersion corrections along with on-the-fly norm-conserving pseudopotentials are employed with 400 eV energy cutoff and 0.02 $Å^{-1}$ spaced Monkhorst-Pack grid for k-point sampling.[53,54] The resulting Pnam symmetric cell has lattice parameters of a = 8.480128 Å, b = 4.126914 Å and c = 10.3203228 Å, which are within 1.7 % of the experimental values for BiSI natural single crystals.[33,55] Raman spectrum is also calculated using CASTEP under density functional perturbation theory (DFPT) linear response formalism.

The electronic structure calculations are performed using single shot GW or the G_0W_0 corrections on a preliminary electronic structure obtained with spin-orbit coupling included hybrid DFT-PBE0 implementation in ABINIT code.[56] The initial DFT calculations are done using norm-conserving pseudopotentials and k-point sampling with 0.02 $Å^{-1}$ spaced Monkhorst-Pack grid. While G_0W_0 calculations are performed within Godby–Needs plasmon-pole approximation while expanding the dielectric matrix with a ~ 400 eV cut off.[57]

The ionization potential (IP) was obtained from electrostatic potential calculations using slab model under DFT-PBE formalism in CASTEP. The as-computed IP is corrected for self-interaction error by adding the quasiparticle correction obtained from the GW calculations, following the approach described by Toroker et al.[43]

ASSOCIATED CONTENT

Supporting Information

Structural parameters of BiSI obtained Rietveld refinement of XRD; Computed effective masses; PV performance parameters of BiSI solar cells; Tauc's plot analysis of BiSI films; Mott-Schottky plot of the SnO_2; BiSI band gap estimation from EQE spectrum of solar cells.

AUTHOR INFORMATION

Corresponding author: David.Fermin@bristol.ac.uk

Notes

The authors declare no competing financial interest.

ACKNOWLEDGMENTS

DT and DJF thank the UK Engineering and Physical Sciences Research Council (EPSRC) for supporting this work through PVTEAM grant (EP/L017792/1). FCD acknowledges the financial support from the Mexican National Council of Science and Technology (CONACYT) while MM is grateful to the support from Chevening Scholarships, the UK government's global scholarship program, funded by the Foreign and Commonwealth Office (FCO) and partner organizations. DT and DJF also acknowledge the fruitful discussions with Prof. N.C. Norman (School of Chemistry, University of Bristol). Scanning electron microscopy and electrochemical impedance spectroscopy were carried out with instrumentation supported by the EPSRC capital grant (EP/K035746/1). Time-resolved PL was carried out at the Wolfson Bioimaging Facility with a fluorescence lifetime imaging microscope (FLIM) acquired under BBSRC/EPSRC-funded

Synthetic Biology Research Centre grant L01386X. We are also grateful to the University of Bristol's supercomputing facilities at the Advanced Computing Research Centre for enabling the computational work.

REFERENCES

(1) Jia, E.; Huang, H.; Wei, D.; Dou, S.; Ji, J.; Li, M.; Cui, P.; Wang, W.; Wang, T. Planar p-n Homojunction Perovskite Solar Cells with Efficiency Exceeding 21.3%. *Nat. Energy* **2019**, *4*, 150–159.

(2) Herz, L. M. Charge-Carrier Dynamics in Organic-Inorganic Metal Halide Perovskites. *Annu. Rev. Phys. Chem.* **2016**, *67*, 65–89.

(3) Brenner, T. M.; Egger, D. A.; Kronik, L.; Hodes, G.; Cahen, D. Hybrid Organic - Inorganic Perovskites: Low-Cost Semiconductors with Intriguing Charge-Transport Properties. *Nat. Rev. Mater.* **2016**, *1*, 15007-1–17.

(4) Frost, J. M.; Butler, K. T.; Brivio, F.; Hendon, C. H.; Van Schilfgaarde, M.; Walsh, A. Atomistic Origins of High-Performance in Hybrid Halide Perovskite Solar Cells. *Nano Lett.* **2014**, *14*, 2584–2590.

(5) Brandt, R. E.; Stevanović, V.; Ginley, D. S.; Buonassisi, T. Identifying Defect-Tolerant Semiconductors with High Minority-Carrier Lifetimes: Beyond Hybrid Lead Halide Perovskites. *MRS Commun.* **2015**, *5*, 265–275.

(6) Ganose, A. M.; Savory, C. N.; Scanlon, D. O. Beyond Methylammonium Lead Iodide: Prospects for the Emergent Field of ns^2 Containing Solar Absorbers. *Chem. Commun.* **2017**, *53*, 20–44.

(7) Bernechea, M.; Miller, N. C.; Xercavins, G.; So, D.; Stavrinadis, A.; Konstantatos, G.

Solution-Processed Solar Cells Based on Environmentally Friendly $AgBiS_2$ Nanocrystals. *Nat. Photonics* **2016**, *10*, 521–525.

(8) Tiwari, D.; Fermin, D. J.; Chaudhuri, T. K.; Ray, A. Solution Processed Bismuth Ferrite Thin Films for All-Oxide Solar Photovoltaics. *J. Phys. Chem. C* **2015**, *119*, 5872–5877.

(9) Whittaker-Brooks, L.; Gao, J.; Hailey, A. K.; Thomas, C. R.; Yao, N.; Loo, Y. L. Bi_2S_3 Nanowire Networks as Electron Acceptor Layers in Solution-Processed Hybrid Solar Cells. *J. Mater. Chem. C* **2015**, *3*, 2686–2692.

(10) Lee, L. C.; Huq, T. N.; MacManus-Driscoll, J. L.; Hoye, R. L. Z. Research Update: Bismuth-Based Perovskite-Inspired Photovoltaic Materials. *APL Mater.* **2018**, *6*, 084502-1–16.

(11) Miller, N. C.; Bernechea, M. Research Update: Bismuth Based Materials for Photovoltaics. *APL Mater.* **2018**, *6*, 084503-1–12.

(12) Tiwari, D.; Alibhai, D.; Fermin, D. J. Above 600mV Open-Circuit Voltage BiI_3 Solar Cells. *ACS Energy Lett.* **2018**, *3*, 1882–1886.

(13) Greul, E.; Petrus, M. L.; Binek, A.; Docampo, P.; Bein, T. Highly Stable, Phase Pure $Cs_2AgBiBr_6$ Double Perovskite Thin Films for Optoelectronic Applications. *J. Mater. Chem. A* **2017**, *5*, 19972–19981.

(14) Kim, Y.; Yang, Z.; Jain, A.; Voznyy, O.; Kim, G. H.; Liu, M.; Quan, L. N.; García de Arquer, F. P.; Comin, R.; Fan, J. Z.; et al. Pure Cubic-Phase Hybrid Iodobismuthates $AgBi_2I_7$ for Thin-Film Photovoltaics. *Angew. Chemie - Int. Ed.* **2016**, *55*, 9586–9590.

(15) Audzijonis, A.; Źigas, L.; Kvedaravicius, A.; Zaltauskas, R. Origin of Ferroelectric Phase Transitions of $Bi_xSb_{1-x}SI$ Mixed Crystals. *Ferroelectrics* **2009**, *392*, 45–54.

(16) Ganose, A. M.; Butler, K. T.; Walsh, A.; Scanlon, D. O. Relativistic Electronic Structure

and Band Alignment of BiSI and BiSeI: Candidate Photovoltaic Materials. *J. Mater. Chem. A* **2016**, *4*, 2060–2068.

(17) Teng, M. K.; Massot, M.; Balkanski, M. Atomic Substitution and Ferroelectric Phase Transition in $Bi_xSb_{1-x}SI$. *Phys. Rev. B* **1978**, *17*, 3695–3700.

(18) Ran, Z.; Wang, X.; Li, Y.; Yang, D.; Zhao, X.-G.; Biswas, K.; Singh, D. J.; Zhang, L. Bismuth and Antimony-Based Oxyhalides and Chalcohalides as Potential Optoelectronic Materials. *npj Comput. Mater.* **2018**, *4*, 14-1–14.

(19) Park, S. -A; Kim, M. -Y; Lim, J. -Y; Park, B. -S; Koh, J. -D; Kim, W. -T. Optical Properties of Undoped and V-Doped V^A–VI^A–VII^A Single Crystals. *Phys. Status Solidi* **1995**, *187*, 253–260.

(20) Wang, K.; Jia, F.; Zheng, Z.; Zhang, L. Crossed BiOI Flake Array Solar Cells. *Electrochem. commun.* **2010**, *12*, 1764–1767.

(21) Zhao, K.; Zhang, X.; Zhang, L. The First BiOI Based Solar Cells. *Electrochem. commun.* **2009**, *11*, 612–615.

(22) Sfaelou, S.; Raptis, D.; Dracopoulos, V.; Lianos, P. BiOI Solar Cells. *RSC Adv.* **2015**, *5*, 95813–95816.

(23) Hoye, R. L. Z.; Lee, L. C.; Kurchin, R. C.; Huq, T. N.; Zhang, K. H. L.; Sponseller, M.; Nienhaus, L.; Brandt, R. E.; Jean, J.; Polizzotti, J. A.; et al. Strongly Enhanced Photovoltaic Performance and Defect Physics of Air-Stable Bismuth Oxyiodide (BiOI). *Adv. Mater.* **2017**, *29*, 1702176-1–10.

(24) Hahn, N. T.; Self, J. L.; Mullins, C. B. BiSI Micro-Rod Thin Films: Efficient Solar Absorber Electrodes? *J. Phys. Chem. Lett.* **2012**, *3*, 1571–1576.

(25) Hahn, N. T.; Rettie, A. J. E.; Beal, S. K.; Fullon, R. R.; Mullins, C. B. N-BiSI Thin Films:

Selenium Doping and Solar Cell Behavior. *J. Phys. Chem. C* **2012**, *116*, 24878–24886.

(26) Chepur, D. V.; Bercha, D. M.; Turyanitsa, I. D.; Slivka, V. Y. Peculiarities of the Energy Spectrum and Edge Absorption in the Chain Compounds $A^{V}B^{VI}C^{VII}$. *Phys. Status Solidi* **1968**, *30*, 461–468.

(27) Aliev, Z. S.; Musayeva, S. S.; Jafarli, F. Y.; Amiraslanov, I. R.; Shevelkov, A. V.; Babanly, M. B. The Phase Equilibria in the Bi-S-I Ternary System and Thermodynamic Properties of the BiSI and $Bi_{19}S_{27}I_3$ Ternary Compounds. *J. Alloys Compd.* **2014**, *610*, 522–528.

(28) Groom, R.; Jacobs, A.; Cepeda, M.; Drummey, R.; Latturner, S. E. $Bi_{13}S_{18}I_2$: (Re)Discovery of a Subvalent Bismuth Compound Featuring $[Bi_2]^{4+}$ Dimers Grown in Sulfur/Iodine Flux Mixtures. *Chem. Mater.* **2017**, *29*, 3314–3323.

(29) Tiwari, D.; Koehler, T.; Lin, X.; Harniman, R.; Griffiths, I.; Wang, L.; Cherns, D.; Klenk, R.; Fermin, D. J. Cu_2ZnSnS_4 Thin Films Generated from a Single Solution Based Precursor: The Effect of Na and Sb Doping. *Chem. Mater.* **2016**, *28*, 4991–4997.

(30) Tiwari, D.; Koehler, T.; Klenk, R.; Fermin, D. J. Solution Processed Single-Phase Cu_2SnS_3 Films: Structure and Photovoltaic Performance. *Sustain. Energy Fuels* **2017**, *1*, 899–906.

(31) Tiwari, D.; Koehler, T.; Lin, X.; Sarua, A.; Harniman, R.; Wang, L.; Klenk, R.; Fermin, D. J. Single Molecular Precursor Solution for $CuIn(S,Se)_2$ Thin Films Photovoltaic Cells: Structure and Device Characteristics. *ACS Appl. Mater. Interfaces* **2017**, *9*, 2301–2308.

(32) Tiwari, D.; Skidchenko, E.; Bowers, J.; Yakushev, M. V; Martin, R.; Fermin, D. J. Spectroscopic and Electrical Signatures of Acceptor States in Solution Processed $Cu_2ZnSn(S,Se)_4$ Solar Cells. *J. Mater. Chem. C* **2017**, *5*, 12720–12727.

(33) Haase-Wessel, W. Die Kristallstruktur Des Wismutsulfidjodids (BiSJ). *Naturwissenschaften* **1973**, *60*, 474.

(34) Arivuoli, D.; Gnanam, F. D.; Ramasamy, P. Growth of Bismuth Sulpho-Iodide Single Crystals from Vapour. *J. Mater. Sci.* **1986**, *21*, 2835–2838.

(35) Arivuoli, D.; Gnanam, F. D.; Ramasamy, P. Growth of SbSI and BiSI from Vapour by Iodine Transport. *Mater. Chem. Phyiscs* **1987**, *16*, 181–188.

(36) Teng, M. K.; Balkanski, M.; Massot, M.; Ziolkiewicz, M. K. Optical Phonon Analysis in the $A_VB_{VI}C_{VII}$ Compounds. *Phys. Status Solidi* **1974**, *62*, 173–182.

(37) Park, S. -A; Kim, M. -Y; Lim, J. -Y; Park, B. -S; Koh, J. -D; Kim, W. -T. Optical Properties of Undoped and Chromium-Doped V^A–VI^A–VII^A Single Crystals. *Phys. Status Solidi* **1995**, *187*, 253–260.

(38) Jackson, W. B.; Kelso, S. M.; Tsai, C. C.; Allen, J. W.; Oh, S. Energy Dependence of the Optical Matrix Element in Hydrogenated Amorphous and Crystalline Silicon. **1985**, *31*, 5187–5198.

(39) Hüser, F.; Olsen, T.; Thygesen, K. S. Quasiparticle GW Calculations for Solids, Molecules, and Two-Dimensional Materials. *Phys. Rev. B* **2013**, *87*, 235132-1–14.

(40) Bruneval, F.; Marques, M. A. L. Benchmarking the Starting Points of the GW Approximation for Molecules. *J. Chem. Theory Comput.* **2013**, *9*, 324–329.

(41) Ganose, A. M.; Matsumoto, S.; Buckeridge, J.; Scanlon, D. O. Defect Engineering of Earth-Abundant Solar Absorbers BiSI and BiSeI. *Chem. Mater.* **2018**, *30*, 3827–3835.

(42) Wang, T.; Daiber, B.; Frost, J. M.; Mann, S. A.; Garnett, E. C.; Walsh, A.; Ehrler, B. Indirect to Direct Bandgap Transition in Methylammonium Lead Halide Perovskite. *Energy Environ. Sci.* **2017**, *10*, 509–515.

(43) Toroker, M. C.; Kanan, D. K.; Alidoust, N.; Isseroff, L. Y.; Liao, P.; Carter, E. A. First Principles Scheme to Evaluate Band Edge Positions in Potential Transition Metal Oxide Photocatalysts and Photoelectrodes. *Phys. Chem. Chem. Phys.* **2011**, *13*, 16644–16654.

(44) Eugster, N.; Fermín, D. J.; Girault, H. H. Photoinduced Electron Transfer at Liquid/Liquid Interfaces. Part VI. On the Thermodynamic Driving Force Dependence of the Phenomenological Electron-Transfer Rate Constant. *J. Phys. Chem. B* **2002**, *106*, 3428–3433.

(45) Uda, M.; Nakamura, A.; Yamamoto, T.; Fujimoto, Y. Work Function of Polycrystalline Ag, Au and Al. *J. Electron Spectros. Relat. Phenomena* **2003**, *88–91*, 643–648.

(46) Inbasekaran, M.; Woo, E.; Wu, W.; Bernius, M.; Wujkowski, L. Fluorene Homopolymers and Copolymers. *Synth. Met.* **2000**, *111*, 397–401.

(47) Lu, Z. H.; Greiner, M. T.; Wang, Z. B.; Tang, W. M.; Helander, M. G. Work Function of Fluorine Doped Tin Oxide. *J. Vac. Sci. Technol. A Vacuum, Surfaces, Film.* **2011**, *29*, 011019-1–4.

(48) Repins, I. L.; Metzger, W. K.; Perkins, C. L.; Li, J. V.; Contreras, M. A. Correlation between Measured Minority-Carrier Lifetime and Cu(In,Ga)Se_2 Device Performance. *IEEE Trans. Electron Devices* **2010**, *57*, 2957–2963.

(49) Zhou, Y.; Wang, L.; Chen, S.; Qin, S.; Liu, X.; Chen, J.; Xue, D.-J.; Luo, M.; Cao, Y.; Cheng, Y.; et al. Thin-Film Sb_2Se_3 Photovoltaics with Oriented One-Dimensional Ribbons and Benign Grain Boundaries. *Nat. Photonics* **2015**, *9*, 409–415.

(50) Kurchin, R. C.; Gorai, P.; Buonassisi, T.; Stevanović, V. Structural and Chemical Features Giving Rise to Defect Tolerance of Binary Semiconductors. *Chem. Mater.* **2018**, *30*, 5583–5592.

(51) Payne, M. C.; Teter, M. P.; Allan, D. C.; Arias, T. A.; Joannopoulos, J. D. Iterative Minimization Techniques for Ab Initio Total-Energy Calculations: Molecular Dynamics and Conjugate Gradients. *Rev. Mod. Phys.* **1992**, *64*, 1045–1097.

(52) Clark, S. J.; Segall, M. D.; Pickard, C. J.; Hasnip, P. J.; Probert, M. I. J.; Refson, K.; Payne, M. C. First Principles Methods Using CASTEP. *Zeitschrift für Krist. - Cryst. Mater.* **2005**, *220* (5/6), 567–570.

(53) Perdew, J. P.; Burke, K.; Ernzerhof, M. Generalized Gradient Approximation Made Simple. *Phys. Rev. Lett.* **1996**, *77*, 3865–3868.

(54) Grimme, S. Semiempirical GGA-Type Density Functional Constructed with a Long-Range Dispersion Correction. *J. Comput. Chem.* **2006**, *27*, 1787–1799.

(55) Demartin, F.; Gramaccioli, C. M.; Campostrini, I. Demicheleite-(I), BiSI, a New Mineral from La Fossa Crater, Vulcano, Aeolian Islands, Italy. *Am. Mineral.* **2010**, *74*, 141–145.

(56) Gonze, X.; Amadon, B.; Anglade, P. M.; Beuken, J. M.; Bottin, F.; Boulanger, P.; Bruneval, F.; Caliste, D.; Caracas, R.; Côté, M.; et al. ABINIT: First-Principles Approach to Material and Nanosystem Properties. *Comput. Phys. Commun.* **2009**, *180*, 2582–2615.

(57) Godby, R. W.; Needs, R. J. Metal-Insulator Transition in Kohn-Sham Theory and Quasiparticle Theory. *Phys. Rev. Lett.* **1989**, *62*, 1169–1172.